OPEN ACCESS
OPUS AUGSBURG

Universität Augsburg
Universitätsbibliothek

3D printing of freestanding MXene architectures for current collector free supercapacitors

Wenji Yang, Jie Yang, Jae Jong Byun, Francis P. Moissinac, Jiaqi Xu, Sarah J. Haigh, Marco Domingos, Mark A. Bissett, Robert A. W. Dryfe, Suelen Barg

Angaben zur Veröffentlichung / Publication details:

Yang, Wenji, Jie Yang, Jae Jong Byun, Francis P. Moissinac, Jiaqi Xu, Sarah J. Haigh, Marco Domingos, Mark A. Bissett, Robert A. W. Dryfe, and Suelen Barg. 2019. "3D printing of freestanding MXene architectures for current collector free supercapacitors." *Advanced Materials* 31 (37): 1902725. https://doi.org/10.1002/adma.201902725.

Nutzungsbedingungen / Terms of use: **licgercopyright**

Dieses Dokument wird unter folgenden Bedingungen zur Verfügung gestellt: / This document is made available under these conditions:
Deutsches Urheberrecht
Weitere Informationen finden Sie unter: / For more information see:
https://www.uni-augsburg.de/de/organisation/bibliothek/publizieren-zitieren-archivieren/publiz/

3D printing of Freestanding MXene Architectures for Current Collector-Free Supercapacitors

Wenji Yang[ζ†], Jie Yang[ζ‡§], Jae Jong Byun[†] Francis Moissinac[†], Jiaqi Xu[†], Sarah J Haigh[†], Marco Domingos[δ], Mark A. Bissett[†], Robert A.W. Dryfe[‡§], Suelen Barg[†*]

† School of Materials, University of Manchester, Oxford Road, Manchester, M13 9PL, U.K.

‡ National Graphene Institute, University of Manchester, Oxford Road, Manchester, M13 9PL, U.K.

§ School of Chemistry, University of Manchester, Oxford Road, Manchester M13 9PL, U.K.

δ School of Mechanical, Aerospace and Civil Engineering, University of Manchester, Oxford Road, Manchester M13 9PL, U.K.

ζ These authors contributed equally to this work.

* Corresponding author

Key words: MXene; Aqueous Inks, Rheology; 3D printing; Supercapacitors

Abstract: Additive Manufacturing (AM) technologies appear to be a paradigm for the scalable manufacture of electrochemical energy storage (EES) devices, where complex three-dimensional (3D) architectures are typically required but hard to achieve using conventional techniques. The combination of these technologies and innovative material formulations that maximize surface area accessibility and ion transport within electrodes while minimizing space are of growing interest. Herein, we formulate aqueous inks composed of atomically thin (1-3 nm) 2D $Ti_3C_2T_x$ with large lateral size of about 8 μm possessing ideal viscoelastic properties for extrusion-based 3D printing of freestanding, high-specific surface area architectures. The MXene inks were 3D printed into interdigitated electrodes to determine the viability of manufacturing energy storage devices. The 3D printed device with active material loading of about 8.5 mg cm^{-2} achieved areal capacitance as high as 2.1 F cm^{-2} at 1.7 mA cm^{-2} and gravimetric capacitance of 242.5 F g^{-1} at 0.2 A g^{-1} with retention of above 90 % capacitance for 10000 cycles. It also exhibited a high energy density of 0.0244 mWh cm^{-2} and power density of 0.64 mW cm^{-2} at a current density of 4.3 mA cm^{-2}. We anticipate that the sustainable printing and design approach developed in this work can be applied to fabricate high performance bespoke multi-scale and

multi-dimensional 3D architectures of functional and structural materials for integrated devices in energy, catalysis and transportation applications.

Main text: The performance and application of electrochemical energy storage (EES) devices increasingly relies on the development of scalable manufacturing routes and innovative materials formulations that can maximize surface area accessibility and ion transport within electrodes while minimizing space and environmental impact. Consequently, Additive Manufacturing (AM) technologies, which are capable of printing three-dimensional (3D) objects and complex structures, offer unique possibilities to bring novel electrode materials into high performance EES devices. Among the AM technologies, continuous extrusion-based 3D printing (also called direct ink-writing or robocasting) is a versatile and cost-effective processing route where the formulation and properties of colloidal inks directly control the printability and architecture of printed parts. It further offers the ability to integrate functional materials of different surface chemistry and dimensionality into EES devices[1] such as Li-ion batteries[2–4], micro-supercapacitors (MSCs)[5,6] and wearable electronics[7,8]. Recently, two-dimensional (2D) transition metal carbides, called MXenes ($M_{n+1}X_nT_x$, with M representing an early transition metal, X representing C and/or N and, T_x representing the terminal functional groups)[9,10], have shown huge potential as electrode materials for supercapacitors.[11,12] Their combination of metallic conductivity, high density (3.8 ± 0.3 g cm^{-3}) and redox active, negatively charged surfaces can lead to superior charge storage and transfer capabilities when compared to other 2D materials. Their surface functional groups (-O, -OH and -F) further render them hydrophilic allowing them to be easily dispersed into aqueous suspensions and inks for processing electrodes using different approaches such as vacuum filtration[10,13], spin coating[14,15], screen-printing[16,17], stamping[18], and spraying[19–21]. While these approaches show the potential of MXene for water-based processing of EES devices, limitations remain with respect to architectural control, scalability or cost-effectiveness that could be addressed by employing 3D printing technologies. Although MXene aqueous inks have been recently employed in commercial pens for direct writing functional films[22], the development of 3D printable MXene inks and their integration into customised 3D device architectures is

still unexplored. In order to realize this challenge, these materials need to be integrated into inks with very specific rheological properties that allow smooth flow through narrow nozzles while still enabling the extruded filaments to retain their shape even after multiple layers are printed. Furthermore, the optimised ink formulation and processing route should allow the properties of the 2D MXene to be efficiently translated to their 3D printed architecture.

Herein, we formulate aqueous inks with 2D $Ti_3C_2T_x$ (the most studied MXene material) with ideal viscoelastic properties for extrusion-based 3D printing of freestanding, high-specific surface area architectures of different size and shapes (**Figure 1**). Previous studies show that high aspect ratio materials with high surface charge, such as clay, Graphene Oxide (GO) and MXene are effective in tuning the rheological properties for wet processing when compared to conventional colloidal systems[23–25]. In particular, the bi-dimensionality of MXenes in combination with their highly negatively charged surfaces and more positive edges[26] render them electrostatic properties and the capability to intercalate water that is similar to some clays[27]. Here we extend this knowledge to develop 3D printable inks solely based on large lateral size, few-layer thick MXene flakes in water without the necessity of using normally employed sacrificial additives[28–31] to control the rheological properties. We further apply the inks to directly print interdigitated symmetric MSCs with a solid electrolyte using $Ti_3C_2T_x$ as both the electrode material and the current collector (CC). This eliminates the need to employ noble metals[32] or other metallic materials used as CC in 3D printed electrode designs[4,26,30]. The electrodes with an active material loading of about 8.5 mg cm^{-2} exhibited an areal capacitance of 2.1 F cm^{-2} and gravimetric capacitance of 242 F g^{-1} at 0.2 A g^{-1}, high power and energy densities and capacitance retention above 90 % for 10000 cycles. While this work represents a feasibility study, we anticipate that this sustainable printing and design approach can be applied to fabricate customized MXene-based architectures and integrated devices for a wide range of applications from energy storage and transfer, catalysis, electromagnetic shielding, environmental cleaning to advanced composite manufacturing.

In order to probe the suitability of 2D MXenes for extrusion-based 3D printing, we synthesised $Ti_3C_2T_x$ flakes that are both large (8 µm average lateral size) and thin (1-3 nm thick) giving a mean length to thickness ratio of approx. 4000 (**Figure 2a-c**, **Figure S1**). During the synthesis (Experimental Section - SI), the Ti_3AlC_2 precursor is selectively etched in a LiF and HCl mixture (with in-situ formation of HF as the etchant) and the subsequent delamination is achieved by the intercalation of water and Li ions within the negatively charged surface resulting in a volume increase as previously described[27]. We followed a less aggressive etching and delamination protocol[34,35], with no sonication steps (**Figure 1a** and **SI**) to allow the synthesis of 2D flakes of preserved lateral size. After purification and centrifugation steps, the large 1-3 nm thick $Ti_3C_2T_x$ flakes can be readily formulated into homogeneous aqueous inks at neutral pH (Zeta potential of -41 mV with standard deviation of 2 mV) (**Figure S2**). A rheological study of the developed inks was subsequently carried out to probe their suitability for 3D printing (**Figure 2d-f**). The ink's viscosity and viscoelastic properties depend on the $Ti_3C_2T_x$ flakes concentration in water and the inks present a clear shear-thinning behaviour as previously reported for 2D materials systems[23,36,37]. The viscosity recovery of the shear-thinning inks over time shows their potential for continuous extrusion during the 3D printing process (**Figure 2e**). By applying alternate low (0.01 s^{-1}) and high (1000 s^{-1}) shear rates to the inks over time we can observe the viscosity drop at higher rates (simulating the extrusion through narrow nozzles) and the instantaneous recovery of viscosity when the shear stress is reduced (simulating post printing recovery of the inks rheological properties). Interestingly, the 15 mg ml^{-1} inks present viscosity values in the order of magnitude as reported for highly concentrated (2.33 g ml^{-1}, 70 wt %)[38] multi-layered $Ti_3C_2T_x$ suspensions, which indicates that high aspect ratio $Ti_3C_2T_x$ flakes are effective in tuning rheology at low concentrations.

The inks viscoelastic fingerprints (**Figure 2f**) show predominantly solid-like behavior with a high storage modulus (G') at the plateau region (region where G' is independent of stress) indicating the formation of a highly percolated $Ti_3C_2T_x$ network. The viscoelastic network breaks and flows when a critical stress is applied (the yield stress at the cross over point between G' and loss modulus (G'')) resulting in a liquid-like behaviour (G'' > G') that enables continuous extrusion through

micrometre-sized nozzles. The magnitude of the elastic modulus and yield stress increases as the inks become more concentrated with 2D flakes, indicating an increase in suitability for shape retention upon continuous extrusion. The elastic modulus and yield stress for inks with 50 mg mL^{-1} concentration reaches 36507 Pa and 206 Pa, respectively, falling within the range for printable inks reported for other systems[2,39–41]. Furthermore, inks with increased material loading maintained sufficient viscoelastic characteristics to be printable and led to a proportional increase in bulk densities of printed parts **(Figure S3)**. These inks can easily flow through narrow nozzles and instantaneously recover their solid-like behaviour, retaining the nozzle's filamentary shape after extrusion. Consequently, it is possible to successfully fabricate 3D architectures by the continuous extrusion of additive-free large $Ti_3C_2T_x$ aqueous inks layer-by-layer following different structural designs (**Figure 2g** and **S4**). Freestanding wet $Ti_3C_2T_x$ 3D woodpile, hollow rectangular prism, interdigitated electrode configurations and other constructs have been 3D printed directly in air with the shapes retained after the printing process.

The wet 3D structures are subsequently freeze-dried to give freestanding $Ti_3C_2T_x$ architectures without the necessity of any further thermal or chemical treatments as are normally required when using additives or GO[28,37,42]. Freeze-drying protects the internal integrity and the external shape of the structures with low shrinkage resulting in $Ti_3C_2T_x$ 3D architectures of well-defined shapes (**Figure 3a-d**) and filaments in the micrometre range. The process parameters, i.e. the nozzle internal diameter, printing speed and pressure, can be tuned in order to obtain printed filaments that are similar to the internal diameter of the nozzle. The SEM micrograph of the micro-lattice structure (**Figure 3a**) shows individual printed filaments of 326 ± 13 µm in diameter forming the interlaced configuration without bending. Side view imaging of the printed rectangular prism (**Figure 3b**) shows the boundaries between individual printed filament layers without any overlap or internal collapse. These results demonstrate the $Ti_3C_2T_x$ inks viscoelastic properties are highly appropriate for 3D printing of freestanding architectures.

Cross-sectional images through the filaments (**Figure 3c-d**) reveal an internal network of $Ti_3C_2T_x$ flakes with interconnected pores in the range of 12 - 35 µm and smaller openings between them in the range of 3 - 5 µm. While porosity can lead to more

accessible surfaces for the electrolyte and improved rate performances, it can also sacrifice the volumetric capacitance and volumetric energy density to some extent[10]. Thus, the optimization of porosity is a big challenge in electrode design.

Our synthesis approach resulted in large, few-layers flakes with a Brunauer-Emmett-Teller (BET) specific surface area (SSA) of 100 $m^2 g^{-1}$ (vacuum dried etched dispersion), which is considerably higher than previously reported (SSA for $Ti_3C_2T_x$ is normally between 4.2 - 55.06 $m^2 g^{-1}$[43–46]). The SSA of the 3D printed $Ti_3C_2T_x$ architectures was calculated as 177 $m^2 g^{-1}$ (**Figure 3g**). The post 3D printing freeze-drying approach assembles the 2D flakes into a porous architecture within the filaments preventing the normal restacking of 2D flakes during drying[47]. This further improves their surface area accessibility compared to conventional techniques (e.g. casting or vacuum filtration). The $Ti_3C_2T_x$ samples present a typical type IV N_2 adsorption/desorption isotherm, indicating their predominantly mesoporous internal structures[48]. Based on the Density Functional Theory model[49], the pore size distribution is determined to be from 0.8 nm to 9 nm (**Figure 3h**). Elemental mapping of the 3D printed $Ti_3C_2T_x$ structures (**Figure S5**) show them to be mainly composed of homogeneously distributed Ti, C, O and F elements and XRD analysis (**Figure S6**) shows very similar peaks to delaminated $Ti_3C_2T_x$ flakes, indicating that the materials do not change crystal structure upon printing and post-printing processes.

In order to demonstrate the potential of our MXene inks for the manufacturing of energy storage devices, we 3D printed interdigitated $Ti_3C_2T_x$ electrodes with tuneable finger thickness and with finger gaps that can be as small as 100 µm (Figures **3e-f** and **S4**). We further assembled symmetrical all MXene solid-state MSCs (using solid electrolyte, a mixture of poly (vinyl alcohol) (PVA) and sulfuric acid) to test the electrochemical performance of 3D printed interdigitated electrode architectures (**Figure 1, 4a-f**, **S7** and **S8**). The assembled demonstrators were composed of about 8.5 mg cm^{-2} active material loaded in 326 µm diameter fingers separated by 187 µm gaps allowing a short distance between electrodes without short-circuiting the devices (**Figure 4a** inset and Figure **S8**). The materials present an ideal capacitive behaviour showing a quasi-rectangular CV curve shape (5 - 20 mVs^{-1}) maintaining a good performance at higher rates (**Figure 4a-b).** The discharging profile in galvanostatic charge-discharge (GCD) curves shows a triangular shape, revealing

typical capacitive characteristics and efficient charge storage ability. The devices present gravimetric capacitances ranging between 242.5 and 117.7 F g^{-1} (for current densities between 0.2 and 5 A g^{-1}, as shown is **Figure S7**) with capacitance retention above 90 % after 10,000 cycles at 1 A g^{-1} (**Figure 4d**).

The kinetics of ion transport and charge transfer in the 3D-printed $Ti_3C_2T_x$ micro-supercapacitor was further investigated by electrochemical impedance spectroscopy (EIS) with a frequency range from 0.01 Hz to 100 kHz. The Nyquist plot shows a semicircle in the high-frequency region and nearly vertical line at the low-frequency region (indicating a good capacitive behaviour and fast ion diffusion). The intercept of the curve with the real axis shows the equivalent series resistance (ESR) of 16.83 Ω (which includes the resistance of the electrode materials, solid electrolyte and contact resistance between the electrode materials with current collector).

The areal capacitance is a critical metric to evaluate the performance of MSCs. The 3D printed devices with active material loading of about 8.5 mg cm^{-2} achieve areal capacitance as high as 2.1 F cm^{-2} at 1.7 mA cm^{-2} and 1.0 F cm^{-2} when the current density is increased by 25 fold (at 42.7 mA cm^{-2}), surpassing the capacitance performance of MXene MSCs produced by other methods (e.g. 42.5 mF cm^{-2} at 0.8 mA cm^{-2})[18]. The Ragone plot (**Figure 4f**) further showcases the potential of 3D printed MXene interdigitated electrodes for high energy density and power density supercapacitors. At a current density of 4.3 mA cm^{-2}, the MSC exhibits an energy density of 0.0244 mWh cm^{-2} and a power density of 0.64 mW cm^{-2}. By increasing the current density to 44 mA cm^{-2}, 50 % of the energy density is retained (0.012 mWh cm^{-2}) while the power density increases to 6.50 mW cm^{-2} (a 10 fold increase). The 3D printed $Ti_3C_2T_x$ MSCs exhibit two orders of magnitude higher energy density with comparable power densities to graphene/CNT hybrids[50]; higher power and energy densities compared to $Ti_3C_2T_X$ supercapacitors[51]; reaching similar performance as RuO_2/ $Ti_3C_2T_X$ hybrid materials[52]. It should be noted that the relatively narrow voltage window limits the energy density to some degree. Therefore, to overcome the voltage window limitation, the use of ionic liquid or organic electrolyte and designing asymmetric supercapacitors with other materials like graphene will be further explored as effective strategies to enhance the energy density.

Conclusion

In this work we have developed additive-free aqueous inks based on large area, thin $Ti_3C_2T_x$ flakes that enable the formation of strong "solid-like" $Ti_3C_2T_x$ networks with ideal rheological properties for layer-by-layer printing of freestanding 3D architectures. The developed manufacturing route enables a good translation of properties from the 2D material into 3D, resulting in architectures with significantly improved SSA compared to other approaches. We have employed the optimized inks to 3D print MSCs with $Ti_3C_2T_x$ interdigitated fingers of tuneable thickness and gap size in the micrometre range. 3D printed devices with a solid electrolyte and active material loading of 8.5 mg cm^{-2} have achieved areal capacitance as high as 2.1 F cm^{-2} at 1.7 mA cm^{-2} with superior energy and power density (e.g. 0.0244 mWh cm^{-2} at 0.64 mW cm^{-2}) compared to previously report symmetric 2D material-based MSCs. The unique rheological properties achieved by the 2D MXene inks combined with the sustainability of the approach can serve as a base to explore other applications requiring controlled 3D architectures and the methodology could be expanded to incorporate other functional and structural materials into MXene-based 3D printable inks. We anticipate that the capability to print customized MXene architectures in three-dimensions that has been demonstrated in this work, will open new opportunities to realise high performance multi-scale and multi-dimensional devices, as required for many different energy, catalysis and transportation applications.

Acknowledgements

The authors would like to thank Huasheng Graphite, UoM (PDS Award), ERC (Starter Grant EvoluTEM) and EPSRC (grants EP/P009050/1, EP/R023034/1 and EP/N032888/1) for the funding.

References

[1] C. W. Foster, M. P. Down, Y. Zhang, X. Ji, S. J. Rowley-Neale, G. C. Smith, P. J. Kelly, C. E. Banks, *Sci. Rep.* **2017**, *7*, 42233.

[2] J. A. Lewis, *Adv. Funct. Mater.* **2006**, *16*, 2193.

[3] K. Sun, T. S. Wei, B. Y. Ahn, J. Y. Seo, S. J. Dillon, J. A. Lewis, *Adv. Mater.* **2013**, *25*, 4539.

[4] T. S. Wei, B. Y. Ahn, J. Grotto, J. A. Lewis, *Adv. Mater.* **2018**, *30*, 1703027.

[5] D. Shen, G. Zou, L. Liu, W. Zhao, A. Wu, W. W. Duley, Y. N. Zhou, *ACS Appl. Mater. Interfaces* **2018**, *10*, 5404.

[6] W. Yu, H. Zhou, B. Q. Li, S. Ding, *ACS Appl. Mater. Interfaces* **2017**, *9*, 4597.

[7] Y. Wang, C. Chen, H. Xie, T. Gao, Y. Yao, G. Pastel, X. Han, Y. Li, J. Zhao, K. K. Fu, L. Hu, *Adv. Funct. Mater.* **2017**, *27*, 1703140.

[8] W. Honda, S. Harada, T. Arie, S. Akita, K. Takei, *Adv. Funct. Mater.* **2014**, *24*, 3299.

[9] B. Anasori, M. R. Lukatskaya, Y. Gogotsi, *Nat. Rev. Mater.* **2017**, *2*, 16098.

[10] M. R. Lukatskaya, S. Kota, Z. Lin, M. Q. Zhao, N. Shpigel, M. D. Levi, J. Halim, P. L. Taberna, M. W. Barsoum, P. Simon, Y. Gogotsi, *Nat. Energy* **2017**, *2*, 17105.

[11] J. Yan, C. E. Ren, K. Maleski, C. B. Hatter, B. Anasori, P. Urbankowski, A. Sarycheva, Y. Gogotsi, *Adv. Funct. Mater.* **2017**, *27*, 1701264.

[12] Y. Wen, T. E. Rufford, X. Chen, N. Li, M. Lyu, L. Dai, L. Wang, *Nano Energy* **2017**, *38*, 368.

[13] Y. Xia, T. S. Mathis, M. Q. Zhao, B. Anasori, A. Dang, Z. Zhou, H. Cho, Y. Gogotsi, S. Yang, *Nature* **2018**, *557*, 409.

[14] G. Ying, A. D. Dillon, A. T. Fafarman, M. W. Barsoum, *Mater. Res. Lett.* **2017**, *5*, 391.

[15] G. Ying, S. Kota, A. D. Dillon, A. T. Fafarman, M. W. Barsoum, *FlatChem* **2018**, *8*, 25.

[16] S. Xu, Y. Dall'Agnese, G. Wei, C. Zhang, Y. Gogotsi, W. Han, *Nano Energy* **2018**, *50*, 479.

[17] H. Hu, T. Hua, *J. Mater. Chem. A* **2017**, *5*, 19639.

[18] C. J. Zhang, M. P. Kremer, A. Seral-Ascaso, S. H. Park, N. McEvoy, B. Anasori, Y. Gogotsi, V. Nicolosi, *Adv. Funct. Mater.* **2018**, *28*, 1705506.

[19] K. Hantanasirisakul, M. Q. Zhao, P. Urbankowski, J. Halim, B. Anasori, S. Kota, C. E. Ren, M. W. Barsoum, Y. Gogotsi, *Adv. Electron. Mater.* **2016**, *2*, 1600050.

[20] A. Sarycheva, A. Polemi, Y. Liu, K. Dandekar, B. Anasori, Y. Gogotsi, *Sci. Adv.* **2018**, *4*, eaau0920.

[21] Z. Wang, H. Kim, H. N. Alshareef, *Adv. Mater.* **2018**, *30*, 1706656.

[22] E. Quain, T. S. Mathis, N. Kurra, K. Maleski, K. L. Van Aken, M. Alhabeb, H. N. Alshareef, Y. Gogotsi, *Adv. Mater. Technol.* **2019**, *4*, 1800256.

[23] B. Akuzum, K. Maleski, B. Anasori, P. Lelyukh, N. J. Alvarez, E. C. Kumbur, Y. Gogotsi, *ACS Nano* **2018**, *12*, 2685.

[24] M. J. Solomon, A. S. Almusallam, K. F. Seefeldt, A. Somwangthanaroj, P. Varadan, *Macromolecules* **2001**, *34*, 1864.

[25] S. Naficy, R. Jalili, S. H. Aboutalebi, R. A. Gorkin, K. Konstantinov, P. C. Innis, G. M. Spinks, P. Poulin, G. G. Wallace, *Mater. Horiz.* **2014**, *1*, 326.

[26] V. Natu, M. Sokol, L. Verger, M. W. Barsoum, *J. Phys. Chem. C* **2018**, *122*, 27745.

[27] M. Ghidiu, M. R. Lukatskaya, M. Q. Zhao, Y. Gogotsi, M. W. Barsoum, *Nature* **2015**, *516*, 78.

[28] E. García-T͡On, S. Barg, J. Franco, R. Bell, S. Eslava, E. D'Elia, R. C. Maher, F. Guitian, E. Saiz, *Adv. Mater.* **2015**, *27*, 1688.

[29] V. G. Rocha, E. García-Tuñón, C. Botas, F. Markoulidis, E. Feilden, E. D'Elia, N. Ni, M. Shaffer, E. Saiz, *ACS Appl. Mater. Interfaces* **2017**, *9*, 37136.

[30] B. G. Compton, J. A. Lewis, *Adv. Mater.* **2014**, *26*, 5930.

[31] W. Wu, A. Deconinck, J. A. Lewis, *Adv. Mater.* **2011**, *23*, H178.

[32] Y. Y. Peng, B. Akuzum, N. Kurra, M. Q. Zhao, M. Alhabeb, B. Anasori, E. C. Kumbur, H. N. Alshareef, M. Der Ger, Y. Gogotsi, *Energy Environ. Sci.* **2016**, *9*, 2847.

[33] W. Li, Y. Li, M. Su, B. An, J. Liu, D. Su, L. Li, F. Li, Y. Song, *J. Mater. Chem. A* **2017**, *5*, 16281.

[34] M. Alhabeb, K. Maleski, B. Anasori, P. Lelyukh, L. Clark, S. Sin, Y. Gogotsi, *Chem. Mater.* **2017**, *29*, 7633.

[35] A. Lipatov, M. Alhabeb, M. R. Lukatskaya, A. Boson, Y. Gogotsi, A. Sinitskii, *Adv. Electron. Mater.* **2016**, *2*, 1600255.

[36] C. Bao, H. Zhang, C. A. Wilkie, S. Bi, X. Z. Tang, J. Wu, J. Yang, *Carbon* **2016**, *107*, 774.

[37] E. García-Tuñón, E. Feilden, H. Zheng, E. D'Elia, A. Leong, E. Saiz, *ACS Appl. Mater. Interfaces* **2017**, *9*, 32977.

[38] B. Akuzum, K. Maleski, B. Anasori, P. Lelyukh, N. J. Alvarez, E. C. Kumbur, Y. Gogotsi, *ACS Nano* **2018**, *12*, 2685.

[39] S. Roh, D. P. Parekh, B. Bharti, S. D. Stoyanov, O. D. Velev, *Adv. Mater.* **2017**, *29*, 1701554.

[40] E. Koos, N. Willenbacher, *Science* **2011**, *331*, 897.

[41] E. García-T͡On, S. Barg, J. Franco, R. Bell, S. Eslava, E. D'Elia, R. C. Maher, F. Guitian, E. Saiz, *Adv. Mater.* **2015**, *27*, 1688.

[42] A. J. Blake, R. R. Kohlmeyer, J. O. Hardin, E. A. Carmona, B. Maruyama, J. D. Berrigan, H. Huang, M. F. Durstock, *Adv. Energy Mater.* **2017**, *7*, 1602920.

[43] Y. Fang, Z. Liu, J. Han, Z. Jin, Y. Han, F. Wang, Y. Niu, Y. Wu, Y. Xu, *Adv. Energy Mater.* **2019**, 1803406.

[44] S. Xu, G. Wei, J. Li, Y. Ji, N. Klyui, V. Izotov, W. Han, *Chem. Eng. J.* **2017**, *317*, 1026.

[45] Y. Zhang, B. Guo, L. Hu, Q. Xu, Y. Li, D. Liu, M. Xu, *J. Alloys Compd.* **2018**, *732*, 448.

[46] L. Wang, H. Zhang, B. Wang, C. Shen, C. Zhang, Q. Hu, A. Zhou, B. Liu, *Electron. Mater. Lett.* **2016**, *12*, 702.

[47] Q. Zhang, F. Zhang, S. P. Medarametla, H. Li, C. Zhou, D. Lin, *Small* **2016**, *12*,

1702.

[48] B. Chen, Z. Zhu, J. Hong, Z. Wen, J. Ma, Y. Qiu, J. Chen, *Dalton Trans.* **2014**, *43*, 10767.

[49] J. Jagiello, M. Thommes, *Carbon* **2004**, *42*, 1227.

[50] M. Beidaghi, C. Wang, *Adv. Funct. Mater.* **2012**, *22*, 4501.

[51] C. J. Zhang, B. Anasori, A. Seral-Ascaso, S. H. Park, N. McEvoy, A. Shmeliov, G. S. Duesberg, J. N. Coleman, Y. Gogotsi, V. Nicolosi, *Adv. Mater.* **2017**, *29*, 1702678.

[52] Q. Jiang, N. Kurra, M. Alhabeb, Y. Gogotsi, H. N. Alshareef, *Adv. Energy Mater.* **2018**, *8*, 1703043.

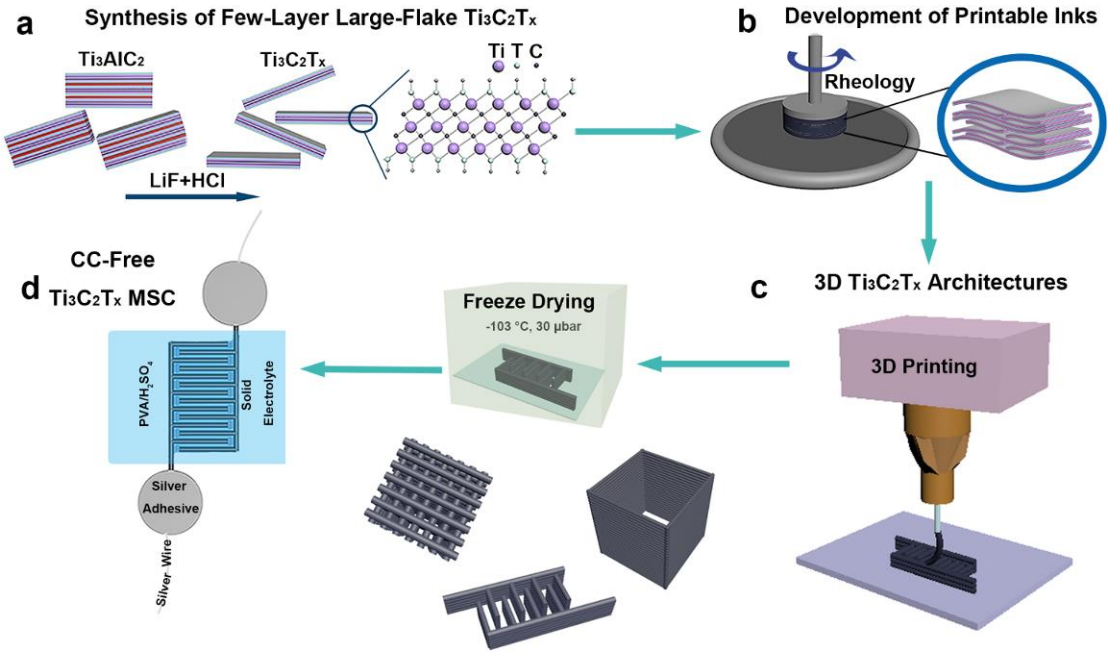

Figure 1. Schematic representation of the manufacturing strategy developed for 3D printing of freestanding MXene architectures and MSC demonstrators. (a) Synthesis of 2D $Ti_3C_2T_x$ following a less aggressive approach with multiple purifications and no sonication steps to allow the formation of few-layers large flakes. (b) Development of $Ti_3C_2T_x$ aqueous inks at neutral pH and study of their suitability for 3D printing via specific rheological characterizations (e.g. viscous properties under shear and their viscoelastic fingerprints); (c) 3D printing of inks with suitable viscoelastic fingerprints layer-by-layer to produce different 3D designs. The subsequent freeze-drying gives rise to freestanding 3D architectures that retain their shape and dimensions; (d) Probing the suitability of the 3D printable inks to develop high performance symmetrical current collector-free (CC-Free) $Ti_3C_2T_x$ solid-state MSCs.

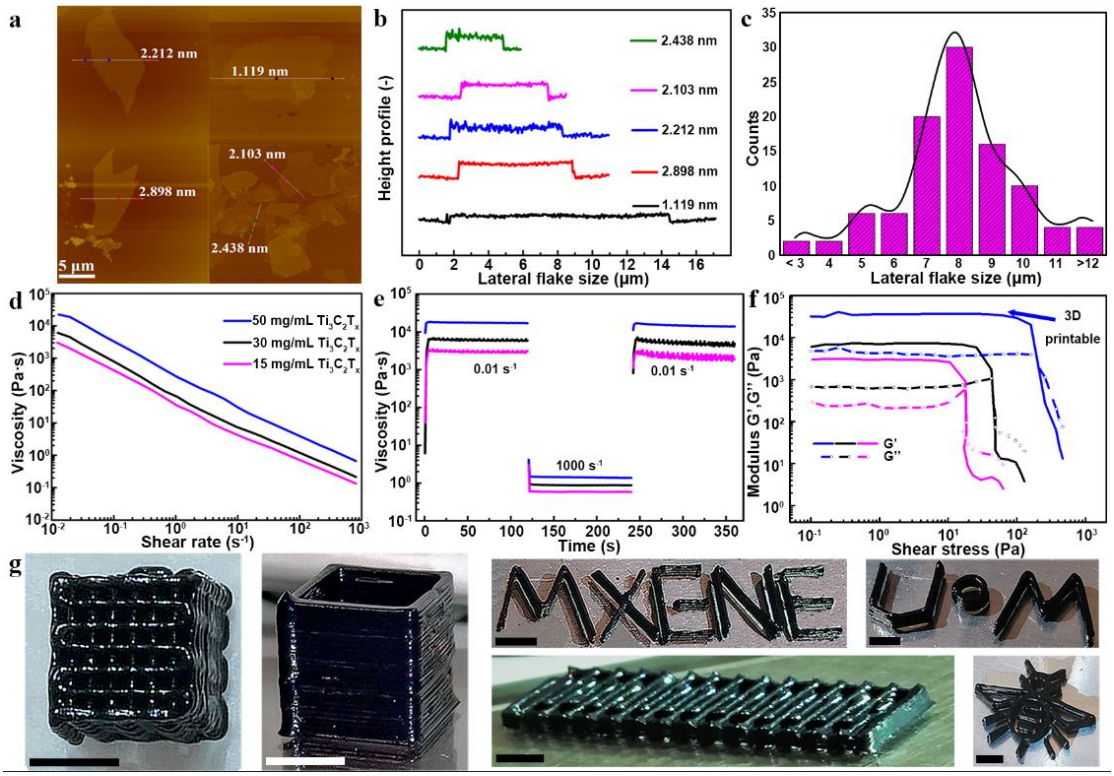

Figure 2. $Ti_3C_2T_x$ flakes dimensional analysis via atomic force microscopy (AFM) (a-b) and scanning electron microscopy (SEM) (c), inks rheological characterization (d-e) and wet stage 3D printed structures (g). a-b) Flake thicknesses ranging from approximately 1 to 3 nm. Large area and thin flakes with aspect ratios above 10000 can be synthesised (a representative 1.1 nm thick, 12 µm lateral size flake is represented by the black line). c) Histogram of $Ti_3C_2T_x$ flakes lateral size obtained from SEM imaging of diluted inks (**Figure S1**). The mean lateral flake size is 8 µm with a standard deviation of 2.7 µm. d) Inks shear thinning behaviour appropriate for continuous extrusion through printing nozzles as narrow as 250 µm diameter. Inset legend refers to line colours used in panels d-f. e) Inks viscosity evolution over time for alternate low (0.01 s^{-1}) and high shear rate (1000 s^{-1}) showcasing appropriate viscosity drop and post-printing recovery. f) Inks viscoelastic fingerprints showing their solid-like behavior with large plateau regions (where G' is independent of stress) and yield stresses (cross over point between G' and G'') that increase as the inks become more concentrated. In particular, 50 mg ml^{-1} inks demonstrate an elastic modulus of 3747 Pa and extendable plateau regions with yield stress of 206 Pa enabling them to be 3D printable. Inks at 15, 30 and 50 mg ml^{-1} correspond to 1.5, 2.9 and 4.8 wt% $Ti_3C_2T_x$, respectively. g) Illustration of 3D printed architectures: clock-wise: 3D printed micro-lattice and rectangular hollow prism printed through 330 and 250 µm nozzles respectively (both 25 printed layers); MXene (4 layers), UoM (5 layers), bee (3 layers) and interdigitated (4 layers) designs all printed through a 330 µm nozzle. All structures used a printing speed of 6 - 10 mm s^{-1}. All scale bars in g) correspond to 3 mm.

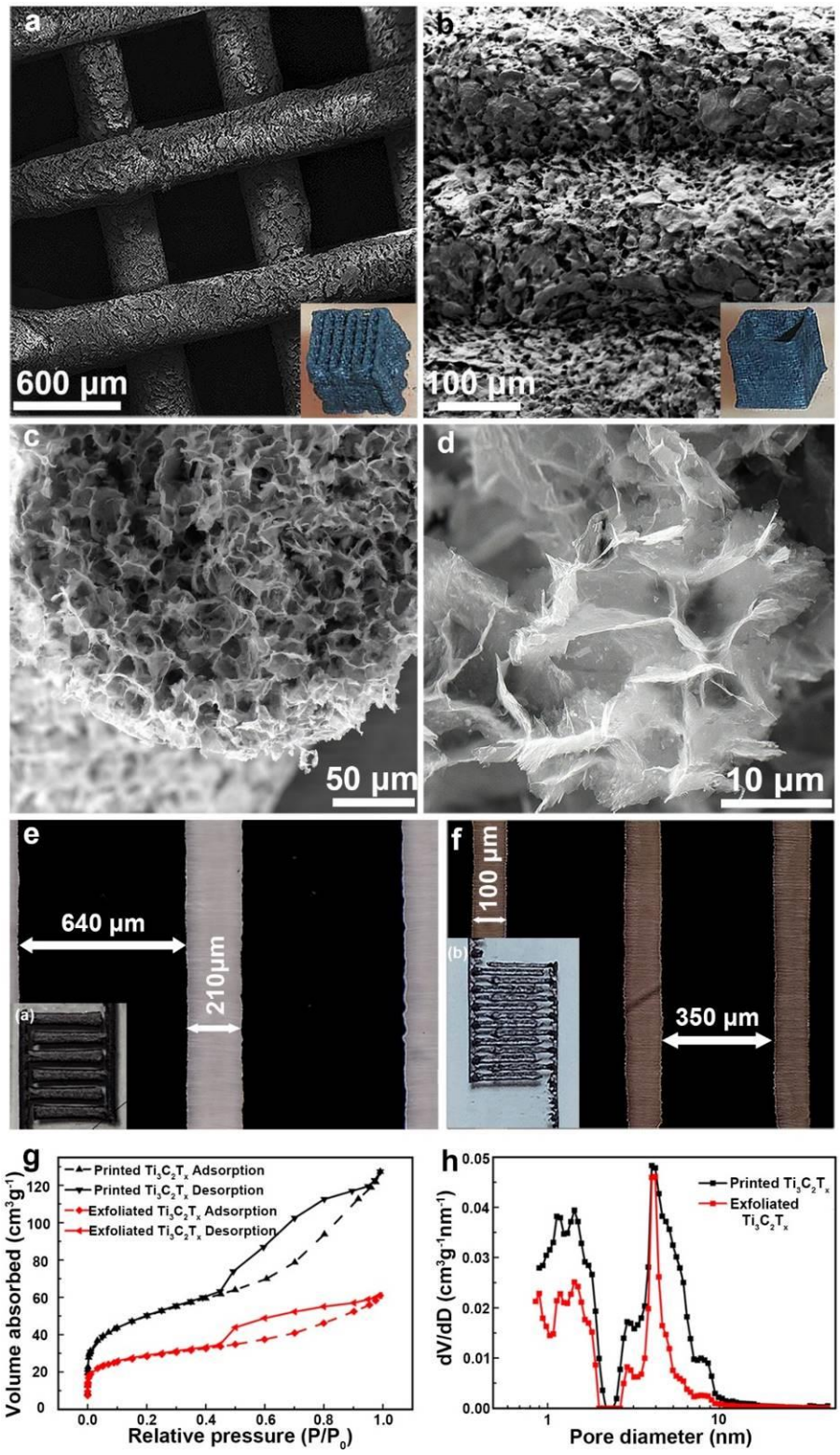

Figure 3. 3D printed multi-scale architectures after freeze-drying. SEM and optical micrographs (inset) of free-standing $Ti_3C_2T_X$ micro-lattice (a) and hollow rectangular prism (b) printed through 330 and 250 µm nozzles, respectively; The cross-sectional SEM images of one filament within the micro-lattice in (a) show the retention of shape and formation of porous internal structures upon freeze-drying (c-d). e-f) Optical micrographs (inset) of 3D printed interdigitated designs with a $Ti_3C_2T_X$ finger thicknesses and finger gaps of 640 and 210 µm (e) and 350 and 100 µm (f),

respectively. g-h) N_2 adsorption and desorption isotherms and the pore size distribution of vacuum dried 2D $Ti_3C_2T_x$ (SSA of 100 m^2g^{-1}) and 3D printed $Ti_3C_2T_x$ architectures (SSA of 177 m^2g^{-1}). The preserved surface area of few-layer and large vacuum dried 2D $Ti_3C_2T_x$ is further improved upon 3D printing and freeze-drying. The inset printed structures in (a), (b), (e) and (f) all have lateral sizes of 5 mm.

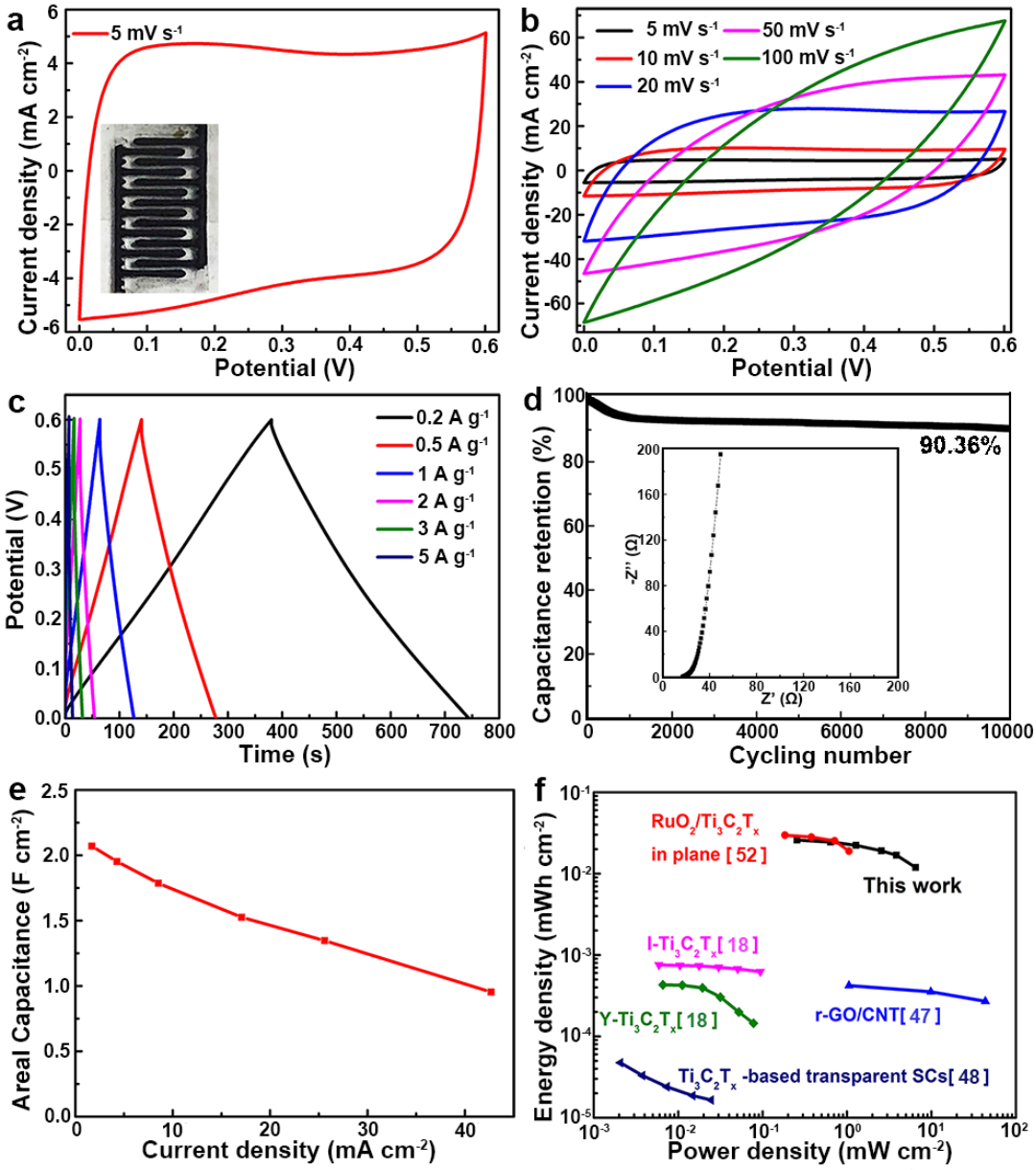

Figure 4. Electrochemical performance of 3D printed few-layer large-flake $Ti_3C_2T_x$ interdigitated electrodes integrated into current-collector free symmetric MSCs (finger diameter of 326 µm and gap distance of 187 µm). a) cyclic voltammetry (CV) at 5 mV s^{-1} showing the ideal capacitive behaviour. The MSC MXene interdigitated electrode configuration is shown in the inset (5 mm smallest lateral size). b) CVs collected at scan rates of 5 mV s^{-1} to 100 mV s^{-1}; c) galvanostatic charge-discharge (GCD) profiles collected at different current densities ranging from 0.2 A g^{-1} to 5 A g^{-1}; d) Cycling stability test showing over 90 % capacitance retention after 10 000 cycles at 1 A g^{-}

[1]. e) Areal capacitance *versus* different areal current densities (2 - 44 mA cm^{-2}); f) Ragone plots of the 3D printed $Ti_3C_2T_x$ supercapacitors together with other reported values for comparison. MSCs tested presented a loading of 8.5 mg cm^{-2}.

ToC

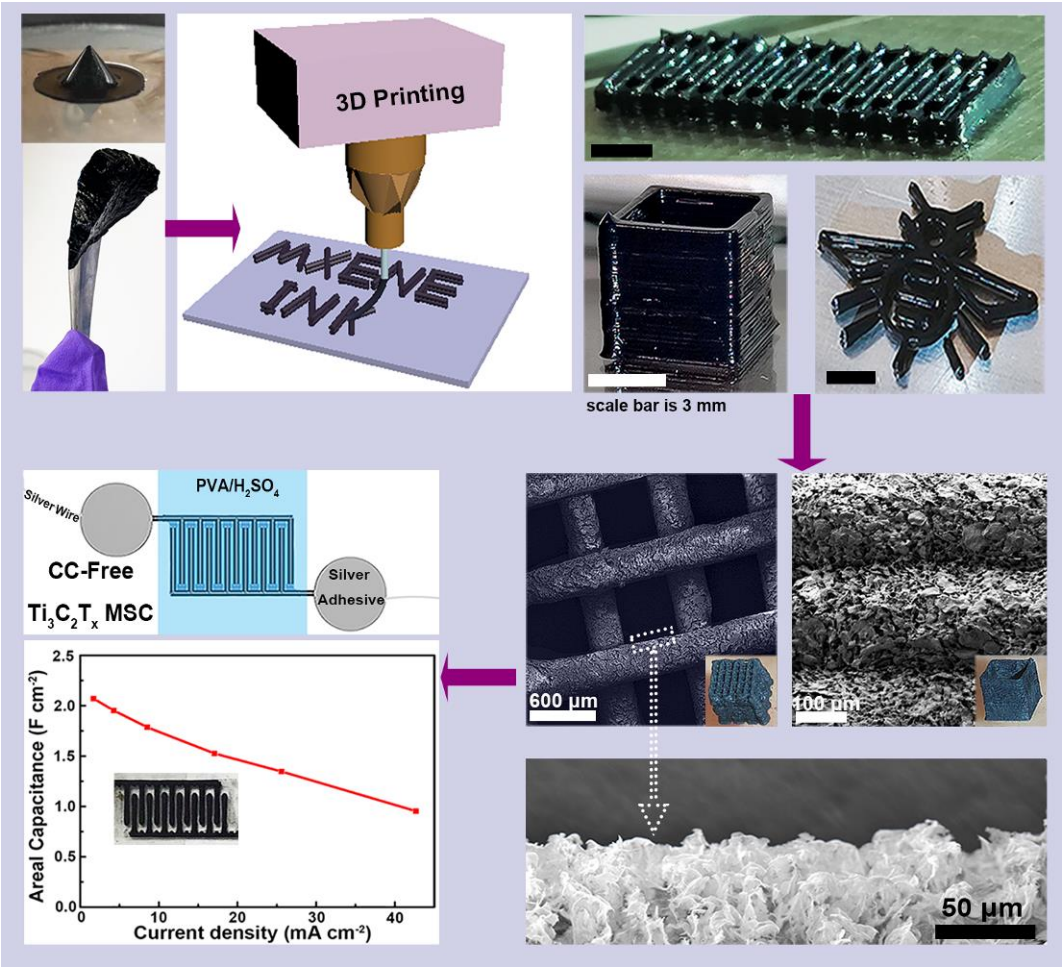

A current collector-free, interdigitated-supercapacitor device is manufactured by 3D printing with water-based MXene ink. Simple modifications to ink synthesis and formulation provided unique rheological properties, which enabled the printability of 3D structures of up to 25 layers high. Final structures demonstrated high specific area, resulting in high areal capacitance of the micro-supercapacitor device.